11. Theory of Atomic-Scale Friction

D. Tománek

With 17 Figures

Friction between two solids is not only one of the most common, but also one of the most complex and least understood processes in nature [11.1]. At rough interfaces, plastic deformations and abrasion – both associated with the re-arrangement of interatomic bonds – are responsible for energy dissipation during the relative motion of the two solids. A fundamentally different behavior is observed at "perfect", weakly-interacting interfaces. There, friction without wear corresponds to energy transfer from macroscopic degrees of freedom (describing the relative motion of the bodies in contact) to microscopic degrees of freedom (such as phonons or electronic excitations) which occur as heat. Considerable success has been achieved recently in the quantitative measurement of friction forces on the atomic scale [11.2] and the understanding of the underlying microscopic mechanisms in the case of sliding friction without wear [11.3]. This success has been made possible by an increasing sophistication in the characterization of interfaces, from the use of rather rough interfaces [11.4, 5] to atomically flat areas [11.6], and imaginative adaptations of the Scanning Force Microscope (SFM) [11.7] for friction measurements. On the other hand, rapid development of computational techniques and the availability of large computer resources have made quantitative predictions for the friction process possible [11.8, 9]. The success on both the experimental and theoretical side has opened up a new research field called *nanotribology*.

In this chapter, I will discuss the new possibilities, but also the limitations of scanning force microscopy in obtaining fundamental understanding of both the *sliding* and *rolling friction* processes. I will start with a brief discussion of the irreversibility in the friction process and possible ways to model an "ideal friction machine" based on the SFM. Next, I will review existing first-principles calculations for friction associated with a single atom sliding on a substrate. Finally, I will discuss limits of nondestructive adsorbate–substrate interactions which are related to the onset of wear in SFM measurements.

11.1 Microscopic Origins of Friction

Let us consider two bodies in contact, A and B, which are in relative motion. Under normal conditions, a friction force F_f occurs in this situation along the direction of motion in addition to the reaction forces of classical mechanics

[11.10]. This force is related to the applied load F_{ext} between the two bodies as

$$F_f = \mu F_{ext} . \tag{11.1}$$

The coefficient of friction, μ, ranges typically between 10^{-2} for smooth interfaces and 1 for rough interfaces. Large values of μ reflect the fact that interatomic bonds at the A–B interface are being broken or rearranged during the relative motion of the bodies. At an interface with essentially flat areas, we can consider several cases which can be classified according to relative bond strengths. This will allow us to establish the conditions under which friction without wear can be expected.

Let us first discuss the basic situations occurring during friction *with wear*. If interatomic A–A bonds are comparable in strength to B–B bonds, and both much weaker than A–B bonds, the relative motion between A and B will eliminate large asperities at the interface in a "sandpaper action". This process is typically accompained by long-ranged plastic deformations and dislocation motion away from the interface. Note that, in this case, a lubricant C is often used [11.11]. The situation of A–B bonds stronger than A–A and B–B bonds will lead to spontaneous bonding at the interface (similar to the case of strong C–C bonds which make C an adhesive). The relative motion of A and B will in this case result from a fracture inside the weaker of the solids along the interface. If B–B bonds are much weaker than A–A bonds, the relative motion of A on B will lead to a "plowing" of B by A.

Friction *without wear* can occur in the ideal case of a defect-free interface between single crystals A and B. In order to avoid plastic deformations, we also require the load F_{ext} on the interface not to exceed the elastic limit within the "softer" solid. Furthermore, the A–A bonds should be comparable in strength to B–B bonds, and at the same time be stronger than A–B bonds. It was recognized a long time ago that, in this case, the only source of friction and its modulation should be atomic-scale corrugations of the A–B interaction potential [11.12].

These modulations and the associated friction force have first been observed successfully on highly oriented pyrolytic graphite using the friction force microscope (FFM) with a tungsten tip [11.2]. As for the theory, two different approaches have been used to determine atomic-scale friction. Molecular dynamics calculations with parametrized pair potentials have been used to simulate the stick–slip motion and to determine the friction force between a Si SFM tip and a Si substrate [11.8]. An independent approach, based on an *ab initio* density functional calculation, has been used to determine the trajectory of a Pd atom moving along a graphite surface and to estimate the associated friction force [11.9].

The variety of processes which are expected to occur during sliding friction can be easily illustrated in a somewhat simple-minded model, namely two haircombs in relative motion, with their teeth (representing surface atoms) in contact. This is shown in Fig. 11.1. "Friction" occurs due to the snapping motion as the teeth slide against each other (Fig. 11.1a). In the case that the teeth are only weakly interlocked, friction energy is dissipated into the vibrations of

Fig. 11.1. Haircomb models illustrating the origin of atomic-scale friction. (**a**) Sliding friction at an "ideal" A–B interface. (**b**) Sliding friction as observed in a friction force microscope (a modified SFM capable of measuring forces in the direction of the trajectory). The teeth of the combs represent atoms at the surface of materials A and B

the teeth of the "softer" comb. In the case of extremely weak interlocking, no snapping motion of the teeth and consequently no friction is expected. No wear occurs in this process. In the case of strong interlocking, individual teeth are likely to break off, corresponding to friction with wear. Without loss of generality, this process can be investigated even if one of the combs has a single tooth left, as shown in Fig. 11.1b. This is the basic model of sliding friction between A and B being investigated by a sharp SFM tip of material A interacting with the substrate B.

The microscopic description of friction without wear must address the fact that friction is a non-conservative process. In other words, the friction force depends on the direction of motion between two bodies in contact and hence can *not* be obtained as a derivative of a potential. A closed-loop integral over such a force yields a nonzero value of the dissipated energy W_f,

$$W_f = \oint F_x(x)\,dx \neq 0 \ . \tag{11.2}$$

The origin of the dependency of the force on the direction of motion is illustrated in Fig. 11.2. The solid line with overhangs in the hatched area can be obtained as a gradient of a potential. The overhangs cause a nonunique relationship between F_x and x. For a given direction of motion between A and B (either the $+x$ or $-x$ direction), the system will follow the trajectory indicated by arrows and thereby undergo a sequence of instabilities. The locations where these
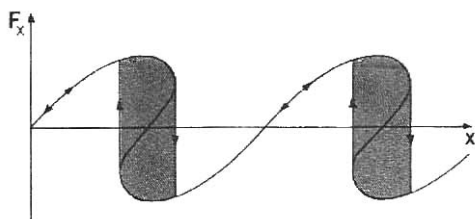

Fig. 11.2. Force F_x on the friction force microscope tip along the trajectory of the scan. Nonzero average value of $\langle F_x \rangle$, corresponding to friction, results from instabilities and non-uniqueness in the F_x versus x relationship

instabilities (or "snapping") occur, depend on the direction of motion. The resulting hysteresis reflects the microscopic irreversibility in the process. The degrees of freedom predominantly involved in the instabilities are those of A or B which are easiest to excite, giving rise to "tip-induced" or "substrate-induced" friction. The energy dissipated in friction, W_f, is related to the hatched area in the hysteresis curve. In the following, we will investigate the microscopic orgin of this hysteresis and discuss friction in a quantitative way.

11.2 Ideal Friction Machines

11.2.1 Sliding Friction

In order to describe friction in a given system better than phenomenologically, we must carefully examine the microscopic processes which lie at the origin of the hysteresis in the "force versus position" curve in Fig. 11.2. I will start the discussion with the sliding friction between an SFM tip and the substrate. After describing the real instrument which is being used to study atomic-scale friction, I will simplify this system to an idealized "Friction Force Microscope" (FFM) which gives rise to sliding friction without wear during a surface scan. I will describe two different models of the FFM which contain the essential physics leading to friction and which I will call "ideal friction machines" [11.13]. These models should be sufficiently realistic to allow a comparison with the experimental equipment described in the following.

One of the first FFM's is a modified scanning force microscope with a tungsten tip which has been used to observe atomic-scale friction without wear on graphite [11.2]. A more recent realization of the friction force microscope [11.14] is shown in Fig. 11.3. Like the SFM, the FFM consists of an "atomically sharp" tip of material A, suspended on a soft cantilever, which is brought into nondestructive contact with a well-defined substrate B. The vertical deflection of the cantilever is regulated in order to keep the applied load F_{ext} constant during the surface scan. The instrument shown in Fig. 11.3 uses the torque on the cantilever due to a horizontal force on the tip to measure the atomic-scale friction force F_f between the tip A and the substrate B. The torsion of the cantilever can be measured independently from F_{ext} by a laser beam which is
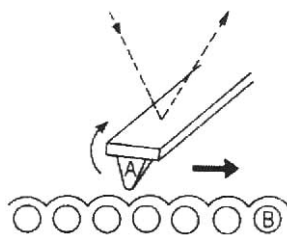

Fig. 11.3. Schematic picture of a friction force microscope. Both vertical motion and torsion of the cantilever are observed by the reflected laser beam
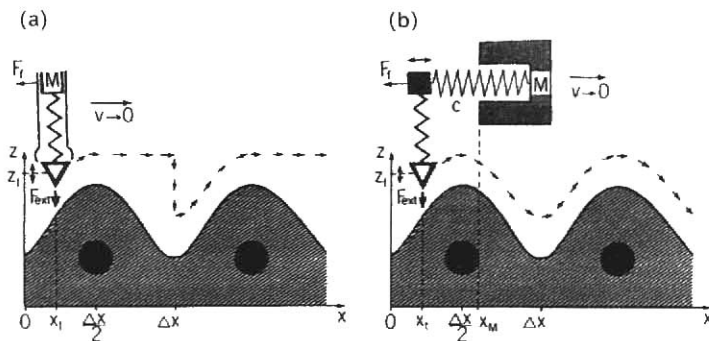
(a)   (b)

Fig. 11.4. Two models of the Friction Force Microscope (FFM). In both models, the external suspension M is guided along the horizontal surface x direction at a constant velocity $v = dx_M/dt \to 0$. The load F_{ext} on the "sharp" tip (indicated by ∇) is kept constant along the trajectory $z_t(x_t)$ (shown by arrows). (a) A "maximum friction microscope", where the tip is free to move up, but gets stuck at the maximum z_t between $\Delta x/2$ and Δx. (b) A "realistic friction microscope", where the position of the tip x_t and the suspension x_M may differ. In this case, the friction force F_f is related to the elongation $x_t - x_M$ of the horizontal spring from its equilibrium value [11.13]

reflected from the cantilever. This experiment gives direct information about F_f as a function of F_{ext}. It is interesting to note that the torque induced by the horizontal force can increase the vertical tip deflection at topographic surface features and hence enhance the contrast of the SFM image.

Two idealized models of a friction force microscope are shown in Fig. 11.4. In both models, the microscope suspension M moves quasi-statically along the surface x-direction with its position x_M as the externally-controlled parameter. The tip is assumed to be stiff in respect to excursions in the surface y-direction. We restrict our discussion to the case of tip-induced friction and assume a rigid substrate which applies for friction measurements on graphite [11.2, 9].

In the "maximum-friction microscope" [11.9], the full amount of energy needed to cross the potential energy barrier ΔV along Δx is dissipated into heat [11.15]. This process and the corresponding friction force can be observed in an imperfect scanning force microscope which is shown in Fig. 11.4a. A vertical spring connects the tip and the external microscope suspension M. The horizontal positions of the tip and the suspension are *rigidly* coupled, $x_t = x_M = x$. For $0 < x < \Delta x/2$, the load F_{ext} on the tip is kept constant by moving the suspension up or down. For $\Delta x/2 < x < \Delta x$, however, the tip gets stuck at the maximum value of z_t. At Δx, the energy ΔV stored in the spring is abruptly and completely released into internal degrees of freedom which appear as heat.

The potential energy $V(x)$ during the sliding process is shown in Fig. 11.5a [11.9]. The force on the tip in the negative x-direction, as defined in Fig. 11.4a, is given by

$$F_f(x_M) = \begin{cases} \partial V(x_M)/\partial x_M & \text{if } 0 < x_M < \Delta x/2 \\ 0 & \text{if } \Delta x/2 < x_M < \Delta x \end{cases} \tag{11.3}$$
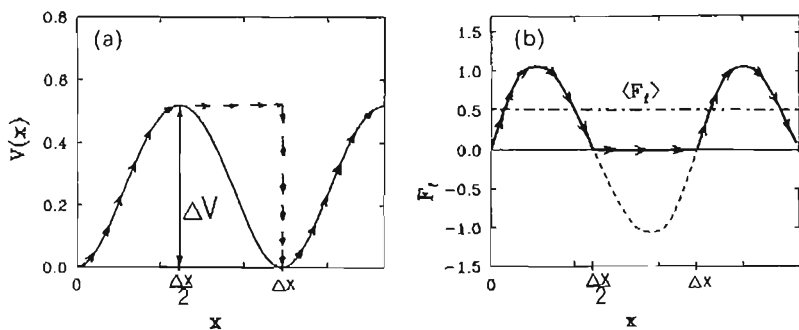
Fig. 11.5. (a) Potential energy of the tip $V(x)$, (b) the friction force $F_f(x)$ and the average friction force $\langle F_f \rangle$ in the "maximum friction" microscope. The arrows indicate the tip trajectory corresponding to a relaxed vertical tip position $z_{t,min}$ for a constant load on the tip [11.13]

and shown in Fig. 11.5b. The non-zero value of the average friction force $\langle F_f \rangle$, indicated by the dash-dotted line in Fig. 11.5b, is a consequence of the mechanism which allows the tip to get stuck. $F_f(x_M)$ is a non-conservative force since it does depend on the scan direction. In absence of the "sticking" mechanism, F_f would be given by the gradient of the potential energy *everywhere*, as indicated by the dashed line in Fig. 11.5b; it would be independent of the scan direction and hence conservative. In such a case, F_f would inhibit sliding for $0 < x_M < \Delta x/2$ and promote sliding for $\Delta x/2 < x_M < \Delta x$. The average value of this force would be zero, resulting in no friction.

A more realistic construction of the friction force microscope is shown in Fig. 11.4b. In this "realistic friction microscope", the SFM-like tip-spring assembly is *elastically* coupled to the suspension in the horizontal direction, so that the horizontal tip position x_t may differ from x_M. While the equilibrium height of the tip, $z_{t,min}(x_t)$, is independent of the scan direction in this model, a "snapping motion" leading to friction can still occur in this instrument, specifically in the case of a soft horizontal spring and a strongly corrugated tip–substrate potential. In the following, I will discuss the conditions for the onset of friction in this model more quantitatively.

For a given x_t, the SFM tip experiences a potential $V(x_t, z_t) = V_{int}(x_t, z_t) + F_{ext} z_t$ consisting of the tip–surface interaction V_{int} and the work against F_{ext}. The tip trajectory $z_{t,min}(x_t)$ during the surface scan is given by the minimum of $V(x_t, z_t)$ with respect to z_t. For this trajectory, $V(x_t) = V(x_t, z_{t,min})$ represents an effective tip–substrate potential. This potential $V(x_t)$ depends strongly on F_{ext} and is corrugated with the periodicity of the substrate due to variations of the chemical bond strength and of $z_{t,min}$, as shown in Fig. 11.6a. The corrugation of the potential $V(x_t)$ will elongate or compress the horizontal spring from its equilibrium which corresponds to $x_t = x_M$. The "instantaneous friction force" is given by
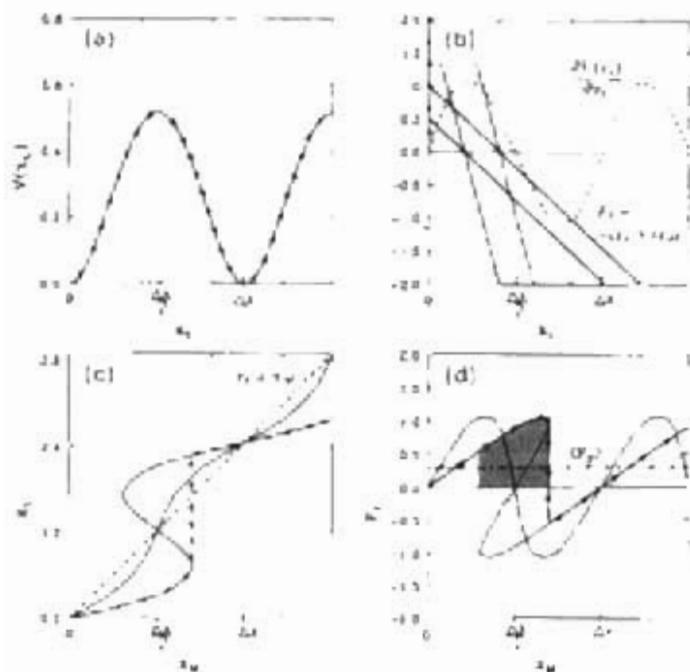
$$F_f(x_M) = -c(x_t - x_M) \ , \tag{11.4}$$

Fig. 11.6. Microscopic friction mechanism in the "realistic friction microscope". Results for a soft spring, giving nonzero friction, are compared to a zero friction microscope with a stiff spring. (a) Potential energy of the tip $V(x_i)$. (b) Graphical solution of (11.7) yielding the equilibrium tip position at the intersection of the derivative of the potential $\partial V(x_i)/\partial x_i$ (dashed line) and the force due to the horizontal spring F_i. Solid lines, for different values of x_M, correspond to a soft spring and dotted lines correspond to a stiff spring. (c) The calculated equilibrium tip position $x_i(x_M)$. (d) The friction force F_i as a function of the FFM position x_M and the average friction force $\langle F_i \rangle$ for the soft spring (dash-dotted line) [11.17]

where c is the horizontal spring constant. The total potential energy V_{tot} of the system consists of $V(x_i)$ and the energy stored in the horizontal spring.

$$V_{tot}(x_i, x_M) = V(x_i) + \tfrac{1}{2}c(x_i - x_M)^2 \tag{11.5}$$

For a given horizontal position x_M of the FFM suspension, the equilibrium position of the tip x_i is obtained by minimizing V_{tot} with respect to x_i. We obtain

$$\frac{\partial V_{tot}}{\partial x_i} = \frac{\partial V(x_i)}{\partial x_i} + c(x_i - x_M) = 0 \tag{11.6}$$

or, with (11.4),

$$F_i = -cx_i + cx_M = \frac{\partial V(x_i)}{\partial x_i} \tag{11.7}$$

A graphical solution of (11.7) is shown in Fig. 11.6b and the resulting relation $x_t(x_M)$ is shown in Fig. 11.6c.

If, for a stiff spring, the force constant c exceeds the critical value $c_{crit} = -[\partial^2 V(x_t)/\partial x_t^2]_{min}$, we obtain a single solution x_t for all x_M. This situation is indicated by the dotted line in Figs. 11.6b, c. The friction force F_f is given by (11.4) and shown by the dotted line in Fig. 11.6d. Since F_f is independent of the scan direction, it is conservative, resulting in $\langle F_f \rangle = 0$. Consequently, we expect no friction to occur during a nondestructive surface scan in a standard SFM which we can consider as a limiting case of the instrument shown in Fig. 11.4b for $c \to \infty$.

A more interesting case arises if the horizontal spring is soft, $c < c_{crit}$. This situation is represented by the solid line in Figs. 11.6b, c. In this case, the solution $x_t(x_M)$ of (11.7) displays a sequence of instabilities. These instabilities lead to a stick–slip motion of the tip as x_M increases, similar to "plucking a string". The hysteresis in the $x_t(x_M)$ relation (Fig. 11.6c) results in a dependence of the force F_f on the scan direction. The friction force $F_f(x_M)$ in this case is shown by the solid line in Fig. 11.6d. It is a nonconservative/dissipative force and averages to a non-zero value of $\langle F_f \rangle$, given by the dash-dotted line. The energy released from the elongated spring into heat is represented by the shaded area in Fig. 11.6d.

The present theory predicts occurrence of friction only for very soft springs or a strongly corrugated potential $V(x_t)$. The latter fact can be verified experimentally since the corrugations $\Delta V(x_t)$ increase strongly with increasing applied load [11.9]. Consequently, for a given c, the friction force is zero unless a minimum load F_{ext} is exceeded. On the other hand, for given F_{ext}, no friction can occur if c exceeds the critical value $c_{crit}(F_{ext})$.

A similar situation occurs during sliding between large commensurate flat surfaces of A on B. In that case, c is given by the elastic constants of A at the interface [11.12], hence can not be changed independently. Since c is rather large in many materials, zero friction should be observed for moderate applied loads in the absence of wear and plastic deformations. For a multi-atom "tip" which is *commensurate* with the substrate, the tip–substrate potential is proportional to the number of tip atoms at the interface, n, as is the critical value c_{crit} for nonzero friction. In this case, the effective FFM spring depends both on the external spring and the elastic response of the tip material. The inverse value of c_{crit} is given by the sum of the inverse values of the corresponding spring constants. For a large tip which is *incommensurate* with the substrate, no friction should occur [11.3].

The average friction force $\langle F_f \rangle$ as a function of the load F_{ext} and the force constant c is shown as a contour plot in Fig. 11.7. Clearly, the applicable load range is limited by the underlying assumption of contact without wear. This figure illustrates that not only the friction force F_f, but also the friction coefficient $\mu = \langle F_f \rangle / F_{ext}$, depend strongly both on the interaction potential between the two materials in contact and on the intrinsic force constant c of the friction force microscope. This clearly makes the friction force dependent on the
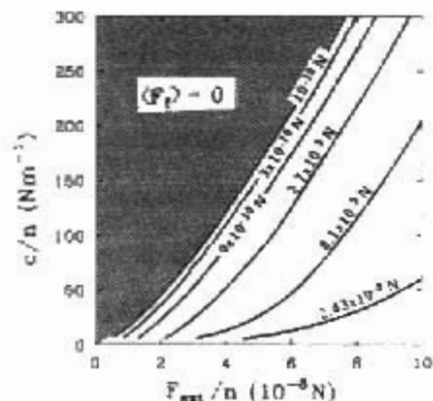
Fig. 11.7. Contour plot of the average friction force $\langle F_r \rangle$ as a function of the load F_{ext} and the force constant c. The calculations are for a monatomic (or a larger commensurate n-atom) Pd tip on graphite. The force constant and all forces are normalized by the number of tip atoms n in contact with the substrate [11.13]

construction parameters of the FFM. There is also one advantage in this fact: c can be chosen in such a way that non-zero friction occurs even at small loads F_{ext}.

11.2.2 Rolling Friction

We have seen that sliding friction is related to a hysteresis in the $x_t(x_M)$ relationship depicted in Fig. 11.6c. As I will discuss in the following, rolling friction is related to a hysteresis in the $z_t(z_M)$ relationship occurring during a vertical approach of an SFM tip to a surface. The corresponding instability has briefly been discussed in Chapter 4 (Volume I, pages 108 ff) and is illustrated

Fig. 11.8. (a) Schematic picture of a scanning force microscope (b) Force on the tip resulting from the interaction with the substrate (solid line) and from the elongated spring (dotted line); (c) Equilibrium tip position z_t as a function of the microscope suspension z_M. The hatched area is proportional to the energy dissipated during one approach-retraction cycle

in Fig. 11.8. The cantilever can be conveniently represented by a vertical spring with a force constant c (Fig. 11.8a). The substrate-induced force on the tip F_t is compensated by the elongated spring,

$$F_t(z_M) = -c(z_t - z_M) \ . \tag{11.8}$$

Here, z_M is the equilibrium tip position in the absence of the substrate. The total potential energy V_{tot} of the system consists of the tip–substrate interaction $V(z_t - z_s) = V(z_t)$ (note that the topmost substrate layer is at $z_s = 0$) and the energy stored in the vertical spring,

$$V_{tot}(z_t, z_M) = V(z_t) + \tfrac{1}{2} c(z_t - z_M)^2 \ . \tag{11.9}$$

For a given position z_M of the tip suspension, the equilibrium position of the tip z_t is obtained by minimizing V_{tot} with respect to z_t. We obtain

$$\frac{\partial V_{tot}}{\partial z_t} = \frac{\partial V(z_t)}{\partial z_t} + c(z_t - z_M) = 0 \tag{11.10}$$

or, with (11.8),

$$F_t = -cz_t + cz_M = \frac{\partial V(z_t)}{\partial z_t} \ . \tag{11.11}$$

A graphical solution of (11.11) is exhibited in Fig. 11.8b and the resulting relation $z_t(z_M)$ is displayed in Fig. 11.8c.

Let us consider a tip approaching the substrate from $z \to \infty$. The force on the tip F_t will be zero first, resulting in $z_t = z_M$, as shown in Fig. 11.8b, c. As the tip slowly approaches the point labeled "1", a deflection towards the surface occurs due to the attractive tip–substrate interaction. At the point labeled "1", the spring can no longer compensate the strong tip–substrate attraction, and the tip jumps to a point labeled "2". The resulting kinetic energy of the tip is dissipated into heat or plastic deformations at the tip–substrate interface. Should the microscope suspension z_M approach the substrate further, the tip will first experience a weakly attractive, then a repulsive interaction with the substrate and will undergo no instabilities. Upon retracting the microscope suspension z_M, the tip will first probe the strongly attractive part of the potential between points "2" and "3". At point "3", the force in the stretched spring can no longer be compensated by the tip–substrate attraction, and the tip jumps to the point labeled by "4". Upon further retracting the microscope suspension z_M, the tip will experience a decreasing attractive interaction from the substrate, resulting in $z_t \to z_M$ with no further instabilities. This is quite analogous to the results presented in Fig. 4.6 for the case of a stationary tip suspension z_M and a moving sample.

Since according to (11.8), $F_t = -c(z_t - z_M)$ is the force on the tip, the hatched area in Fig. 11.8c is proportional to the energy dissipated during an

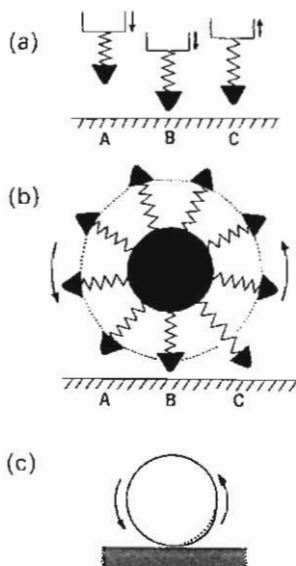

Fig. 11.9. Approach-retraction cycle of (a) a single SFM tip and (b) an array of tips attached to a cylinder rolling on a substrate. The relation of these models to rolling friction between a solid cylinder and a substrate, shown in (c), is discussed in the text

approach-retraction cycle of an SFM tip. This A–B–C–A cycle, which is illustrated in Fig. 11.9a for a single SFM tip, occurs during a revolution by $\Delta\phi$ of a rolling cylinder which has a set of SFM tips attached to the surface, as shown in Fig. 11.9b. The latter is, as a matter of fact, a reasonable model for the energy dissipation at the surface of a solid cylinder, once we associate SFM tips with surface atoms. The corresponding cylinder, which can be imagined as covered by sticky tape and rolling on a substrate, is shown in Fig. 11.9c. The analogy between the cylinder and the SFM is based on the fact that the surface layer of the cylinder interacts with the substrate by Lennard–Jones type potentials, and is kept in place by harmonic forces, same as the SFM tip in Fig. 11.8a.

We conclude that the microscopic origin of *rolling friction* without wear lies in the hysteresis in the $z_t(z_M)$ relation in Fig. 11.8c. Consequently, the microscopic mechanism which transfers macroscopic rotational energy from the cylinder into microscopic degrees of freedom (heat) can be studied quantitatively by measuring the energy dissipated during a single approach-retraction cycle of an SFM tip.

11.3 Predictive Calculations of the Friction Force

11.3.1 Tip–Substrate Interactions in Realistic Systems: Pd on Graphite

As I discussed above, a quantitative study of sliding or rolling friction is possible, once the interaction potential V at the interface between material A and material

B is known accurately enough. In this section, I want to illustrate how for a model system, namely a Pd FFM tip interacting with a graphite substrate, this interaction can be calculated from first principles.

Graphite is an ideal substrate for the study of friction since the binding energy of adsorbed atoms and the variations thereof along the surface are negligibly small near the equilibrium adsorbate–substrate separation. This is specifically true for the Pd-graphite interaction, which is depicted in Fig. 11.10a for the on-top (T) and the sixfold hollow (H) site as a function of the Pd-graphite separation [11.9]. The adsorption energies E_{ad} of Pd atoms (representing the Pd monolayer) in the two adsorption sites on graphite have been defined as $E_{ad} = E_{total}(Pd/graphite) - E_{total}(Pd) - E_{total}(graphite)$. The first-principles total energy calculations for this system have been performed using the Density Functional Formalism within the Local Density Approximation (LDA) [11.17] and the *ab initio* pseudopotential local orbital method [11.18]. The details of the calculation have been discussed in [11.9]. The surface of hexagonal graphite has been represented by a 4-layer slab and the adsorbate by a monolayer of Pd atoms in registry with the substrate (1 Pd atom per surface Wigner–Seitz cell of graphite). The valence charge density of the system is shown in Fig. 11.10b.

For a realistically large and sharp SFM tip, the tip–substrate interaction is likely to be modified by the long-range van der Waals force which is not reproduced correctly by LDA. The van der Waals force between an extended conical tip and a flat surface is estimated using the expression
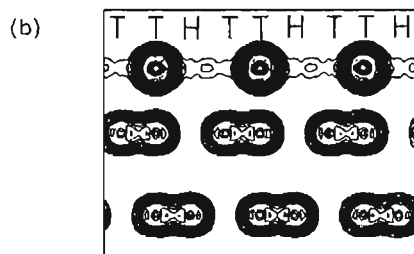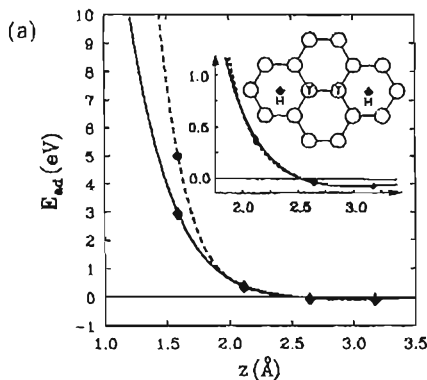

Fig. 11.10. (a) Pd adsorption energy E_{ad} as a function of the adsorption height z above the surface of hexagonal graphite. The solid lines connecting the data points given by ◆ are for the sixfold hollow (H) sites, and the dashed lines connecting the data points given by ● are for the on-top (T) sites. An enlarged section of the graph near equilibrium adsorption is shown in the inset. A second inset shows the adsorption geometry and a possible trajectory of the Pd layer along x in top view. (b) Valence charge density of the Pd/graphite system. The results of the LDA calculation are for the on-top adsorption site near the equilibrium adsorption distance z_{eq}, and are shown in the xz-plane perpendicular to the surface. The ratio of two consecutive charge density contours $\varrho(n + 1)/\varrho(n)$ is 1.2 [11.9, 16]

$F_{\mathrm{vdw}}(z) = A_{\mathrm{H}} \times \tan^2 \alpha/(6z)$, where α is half the opening angle of the tip cone [11.19]. In this expression, A_{H} is the Hamaker constant and z is the distance between the conical tip and the surface. As typical values for a metal tip, one can assume $\alpha = 30°$ and $A_{\mathrm{H}} = 3 \times 10^{-19}$ J. For tip–substrate distances $z > 3$ Å, the van der Waals forces are very small, typically $F_{\mathrm{vdw}} < 10^{-10}$ N. At smaller distances, these forces can be neglected when compared to the closed-shell and internuclear repulsion which are both described correctly within LDA. Since each of these regions is dominated by only one type of interaction, the total tip–substrate force F_{ext} can be approximated as a superposition of the force described by LDA and the van der Waals force. It turns out that the van der Waals forces are not very important for the interpretation of experimental results, since they do not show atomic resolution [11.20] and are easily compensated in the experiment by adjusting the force on the cantilever which supports the tip.

From Fig. 11.10a we see that the equilibrium adsorption bond strength of ≤ 0.1 eV is very weak and much smaller than the cohesive energy of the tip material (Pd metal) or the graphite substrate, which is an important prerequisite for friction with no wear. Near the equilibrium adsorption height $z \approx 3$ Å, the corrugation of the graphite charge density is negligibly small due to Smoluchowski smoothing [11.21] and the position-dependence of the adsorption bond strength is $\ll 0.1$ eV [11.22], which should result in a very small friction coefficient. This calculation indicates that at bond lengths $z \leq 2$ Å, the hollow site is favored with respect to the on-top site. At $z \approx 2$ Å, the adsorption energies are nearly the same and, at larger distances, it is the on-top site which is slightly favored by < 0.05 eV. This is consistent with the dominant interaction changing from closed-shell repulsion (which strongly favors the hollow site at very small adsorption bond lengths) to a weak chemisorption bond (which is stabilized by the hybridization with p_z orbitals in the on-top site). As I will discuss later, the change of the preferential adsorption site from the on-top to the hollow site as a function of the applied load leads to an anomaly in the friction coefficient μ.

A prerequisite for the calculation of the friction force is the precise knowledge of the Pd adsorption energy $E_{\mathrm{ad}}(x, z)$ along the whole graphite surface. Since the corresponding *ab initio* calculations are computationally very expensive, it is useful to find simpler ways to determine this quantity. Several simple potentials have been used for this purpose so far [11.23–25]. Since small inaccuracies in the interaction potentials have a large effect on the friction force, a safer way is to parametrize existing LDA results in a way which makes an evaluation of E_{ad} very easy everywhere. This can be achieved by approximating E_{ad} by a local function which depends only on the total charge density of the graphite host at the Pd adsorption site [11.26],

$$E_{\mathrm{ad}}(r) = E_{\mathrm{ad}}(\varrho(r)) \ . \tag{11.12}$$

This form of the interaction potential is inspired by the density functional formalism [11.17] and the embedded atom method [11.27] and hence is
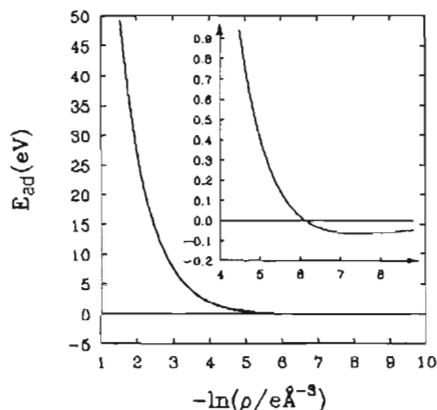
Fig. 11.11. Relation between the Pd adsorption energy $E_{ad}(r)$ and the total charge density of graphite $\varrho(r)$ at the adsorption site r, given by (11.13). An enlarged section of the graph near equilibrium adsorption is given in the inset [11.26]

expected to be quite general, not restricted to the Pd-graphite system. A convenient parametrization of $E_{ad}(\varrho(r))$ is

$$E_{ad}(\varrho(r)) = \varepsilon_1 (\varrho/\varrho_0)^{\alpha_1} - \varepsilon_2 (\varrho/\varrho_0)^{\alpha_2} \ . \tag{11.13}$$

In the case of Pd on graphite, $\varepsilon_1 = 343.076\,\text{eV}$, $\varepsilon_2 = 2.1554\,\text{eV}$, $\alpha_1 = 1.245$, $\alpha_2 = 0.41806$, and $\varrho_0 = 1.0\,\text{e/Å}^3$. The dependence of E_{ad} on ϱ, obtained using the parametrized form in (11.13), is depicted in Fig. 11.11.

In many cases, the total charge density can be well approximated by a superposition of atomic charge densities,

$$\varrho(r) = \sum_n \varrho_{at}(r - R_n) \ . \tag{11.14}$$

This parametrization is especially convenient in case of deformed surfaces where an LDA calculation is difficult due to reduced symmetry. On flat graphite
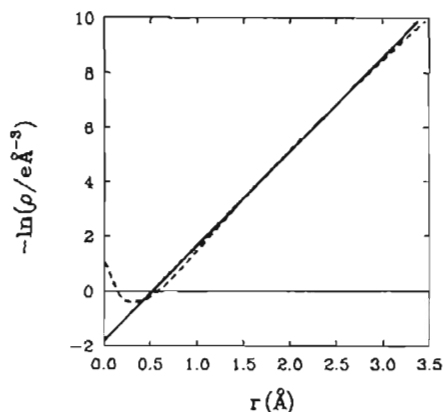

Fig. 11.12. Radial plot of the charge density of a carbon atom $\varrho_{at}(r)$, based on LDA (dashed line). The solid line shows the parametrized form of the charge density, given by (11.15) [11.26]

surfaces, the maximum difference between the LDA charge density and the superposition of atomic charge densities is only a few percent.

Finally, the LDA charge density of the substrate (carbon) atoms can be conveniently expressed as

$$\varrho_{at}(r) = \varrho_C e^{-\beta r} , \tag{11.15}$$

where $\varrho_C = 6.0735$ e/$Å^3$ and $\beta = 3.459$ $Å^{-1}$. As shown in Fig. 11.12, this fit represents the LDA results very well.

11.3.2 Atomic-Scale Friction in Realistic Systems: Pd on Graphite

In the following, I will discuss the atomic-scale friction between a monatomic Pd FFM tip and graphite, based on the "maximum friction microscope" model illustrated in Fig. 11.4a. I will show how the interaction potential between a Pd monolayer and graphite (Pd in registry with the substrate), which has been given in Sect. 11.3.1, can be used to estimate the friction force (and friction coefficient μ) as a function of the applied load.

For a microscopic understanding of the friction process, let us first consider the motion of the Pd layer along the graphite surface, under the influence of an external load per atom [11.28] f_{ext} which is normal to the surface. Following [11.9], we consider a straight trajectory along the surface x direction connecting nearest neighbor sixfold hollow sites on graphite, which are separated by Δx and connected by a bridge site.

As mentioned in the description of the "maximum friction microscope" in Sect. 11.2.1 and shown in Fig. 11.4a, the horizontal positions of the tip and the microscope suspension are the same, $x_t = x_M = x$. The potential energy V of the system along this trajectory has two main components. The first consists of variations of the tip–surface interaction (or adsorption bond energy) $V_{int}(x, z_t) = E_{ad}(x, z_t)$. The second is given by the work against the external load f_{ext} applied on the apex atom of the tip, due to the variations of the tip–substrate distance (or adsorption bond length). Hence,

$$V(x, f_{ext}) = E_{ad}(x, z_{t, min}(x)) + f_{ext} z_{t, min}(x) - V_0(f_{ext}) . \tag{11.16}$$

Here, the potential energy has been set to zero at the hollow site by defining

$$V_0(f_{ext}) = E_{ad}(x_H, z_{t, min}(x)) + f_{ext} z_{t, min}(x_H) . \tag{11.17}$$

The equilibrium tip height $z_{t, min}(x)$ along the trajectory can be determined from

$$f_{ext} = -\frac{\partial}{\partial z} E_{ad}(x, z) . \tag{11.18}$$

In Fig. 11.13a, $V(x)$ is shown for different external loads. We find that the variations of V are dominated by the mechanical component and only partly compensated by the site-dependence of the adsorption energy. As a result of the
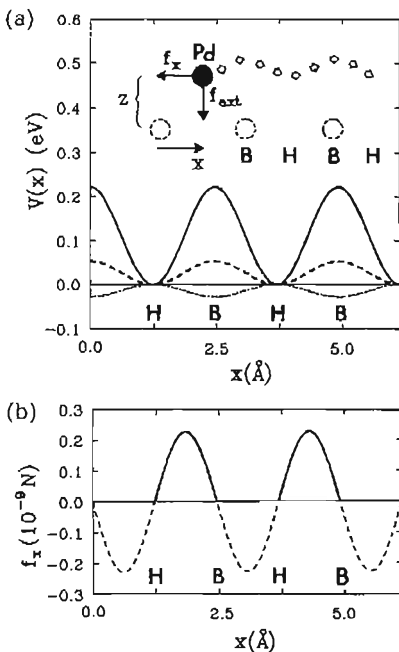
Fig. 11.13. (a) Potential energy $V(x)$ of the Pd-graphite system as a function of the position of the Pd layer along the surface x-direction, for external forces $f_{ext} = 3 \times 10^{-9}$ N (*dotted line*), 6×10^{-9} N (*dashed line*) and 9×10^{-9} N (*solid line*). The inset shows the adsorption geometry and trajectory of the Pd layer in side view. (b) Atomic-scale structure of the force along the surface f_x (*dashed line*) and the friction force $f_f = \max(f_x, 0)$ (*solid line*) for $f_{ext} = 9 \times 10^{-9}$ N [11.9]

variations of V along x, there is a position-dependent force f_x along the x direction. In analogy to (11.3), this force is given by

$$f_x(x, f_{ext}) = \frac{\partial}{\partial x} V(x, f_{ext}) \tag{11.19}$$

and shown in Fig. 11.13b. The maximum value of f_x describes the static friction governing the onset of stick–slip motion. Non-zero average sliding friction comes from the nonconservative "sticking mechanism" of this particular FFM, which is illustrated in Fig. 11.4a and which results in zero horizontal force on the tip for $\Delta x/2 < x < \Delta x$ (see (11.3)). In order to estimate the friction force along the trajectory, we note that the energy loss due to friction W_f along Δx can not exceed the activation energy corresponding to the largest change of V, hence

$$W_f \leq \Delta V_{max} \ . \tag{11.20}$$

Let us now assume that at Δx, the entire energy stored in the spring gets transferred into surface phonons and electron–hole pairs [11.15], as indicated in Fig. 11.4a. Then, both sides of (11.20) will be equal. The horizontal force on the tip will show atomic-scale structure and will not average to zero, as indicated in Figs. 11.5b and 11.13b. This has been observed recently using the FFM [11.2].

The energy W_f dissipated in friction along the trajectory Δx can be used to define the average friction force $\langle f_f \rangle$ as

$$W_f = \langle f_f \rangle \Delta x \ , \tag{11.21}$$

or, using (11.20) for W_f,

$$\langle f_f \rangle = \frac{1}{\Delta x} \Delta V_{max} \ . \tag{11.22}$$

The friction coefficient μ, defined in (11.1), can now be estimated as

$$\mu = \frac{\langle f_f \rangle}{f_{ext}} = \frac{\Delta V_{max}}{f_{ext} \Delta x} \ . \tag{11.23}$$

In Fig. 11.14, μ is shown as a function of f_{ext}. We find a general increase of μ with increasing external force, in contradiction to the general notion that μ is nearly independent of the load. The minimum in $\mu(f_{ext})$ near $f_{ext} = 5 \times 10^{-9}$ N is caused by the switching of the minima in $V(x)$ from H to B, depicted in Fig. 11.13a [11.29].

The above estimates of μ have been obtained for an infinitely rigid substrate, an assumption which holds only within a limited load range. Theoretical results of [11.16, 30], which will be summarized in Sect. 11.4, indicate that if the external force (per atom) exceeds 10^{-8} N, the graphite surface is very strongly deformed [11.31] and likely to be ruptured [11.6]. Since no plastic deformations have been observed in the SFM/FFM studies [11.2], the applied forces were probably in the region $f_{ext} < 10^{-8}$ N. For these values of f_{ext}, the above results for the friction coefficient of $\mu \approx 10^{-2}$ agree with the experimental value [11.2,6].

In order to obtain a meaningful comparison with observable friction forces, we have to make further assumptions about the macroscopic tip–substrate
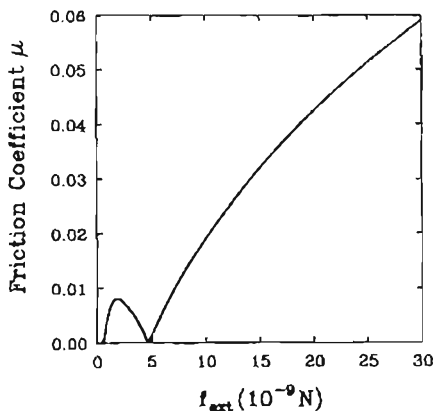

Fig. 11.14. Microscopic friction coefficient μ as a function of the external force per atom f_{ext} [11.9]

interface and the elastic response of the substrate to external forces. In the simplest case, we consider an atomically flat interface, where n atoms are in contact with the substrate, and neglect elastic deformations. Then, the external force per atom f_{ext} is related to the total external force F_{ext} by

$$f_{ext} = \tfrac{1}{n} F_{ext} . \tag{11.24}$$

In Fig. 11.15 we use the calculated $\mu(f_{ext})$ to plot the total friction force F_f for such a perfectly flat interface consisting of 1500 Pd atoms. Since μ increases with increasing value of f_{ext}, the F_f versus F_{ext} relationship is non-linear, which has also been observed in the SFM experiment [11.2].

At this point, it is important to address the validity range of the above calculations. Obviously, the implicit assumption of an infinitely rigid substrate will remain realistic only for limited loads F_{ext} applied on the tip, especially in the case of graphite. Also, there is a critical load for each system which marks the onset of plastic deformations within either the substrate or the tip. The latter point will be discussed in more detail in the following section. Here, I would like to discuss a simple modification of the above results for friction in the case of an extended tip and an elastic substrate.

In the case of large external forces and an elastic substrate such as graphite, linear elasticity theory predicts [11.32] the substrate deformations to be proportional to $F_{ext}^{1/3}$. In the case of a spherical tip [11.2], the tip–substrate interface area and the corresponding number of atoms in contact at the interface are proportional to $F_{ext}^{2/3}$. Then, the force per atom f_{ext} is proportional to $F_{ext}^{1/3}$. Hence for increasing external forces, variations of the effective force per atom and of μ are strongly reduced due to the increasing interface area. This is illustrated by the dashed line in Fig. 11.15, which is based on the assumption that $n = 1500$ tip atoms are in contact with the substrate at $F_{ext} = 10^{-6}$ N. These results are in good agreement with the FFM results for a large nonspecific tungsten tip with a radius $R = 1500$ Å–3000 Å on graphite [11.2], but show
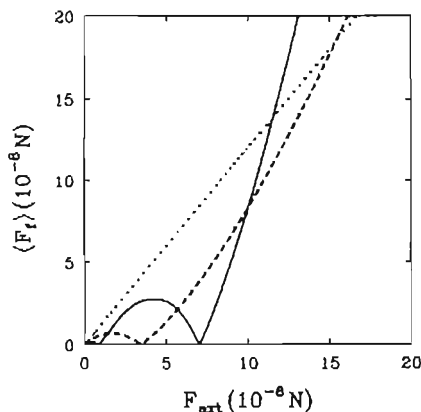

Fig. 11.15. Macroscopic friction force F_f as a function of the external force F_{ext} for a large object. The solid line describes a "flat" object, the surface of which consists of 1500 atoms in contact with a rigid substrate. The dashed line describes a large spherical tip and also considers the effect of elastic substrate deformations on the effective contact area. The dotted line corresponds to a constant friction coefficient $\mu = 0.012$ [11.9]

a slightly larger increase of the friction force than that observed for the range of external forces investigated.

It is instructive to discuss some consequences of the above theory for atomic-scale friction. At rough interfaces, the friction coefficient μ generally increases due to the onset of plastic deformations or wear associated with bond breaking at the interface. It is interesting to note that even in the case of no wear, the above theory would predict an increased value of μ at a rough interface, since the number of atoms n in contact with the substrate is smaller in that case, which would lead to an increase of f_{ext} and hence of μ. Also, with increasing relative velocity between the bodies in contact, the coupling between macroscopic and internal microscopic degrees of freedom (phonons, electron–hole pairs) gets less efficient. Then, $W_f < \Delta V_{max}$ in (11.20), which should result in a decrease of $\langle f_f \rangle$ and μ.

11.4 Limits of Non-destructive Tip–Substrate Interactions in Scanning Force Microscopy

The operating load range of the SFM (and hence the FFM) is limited in two ways. If the applied load on the tip is too small, atomic-scale modulations of the tip–substrate distance z_t and of the horizontal force on the tip f_x will lie below the detection limit. If the load is too large, the substrate and/or the tip will be destroyed. The optimum operating range can be predicted, once the tip–substrate interaction potentials and the elastic properties of the tip and the substrate are known.

Some of these questions have been addressed previously in calculations of the interaction between an infinite "periodic" carbon or aluminium tip and a rigid surface [11.33]. Other calculations have considered the interaction between a single SFM tip and an elastic surface represented by a semi-infinite continuum [11.30] or by a model system of finite thickness [11.25, 34]. In the following, I will show, how this optimum load operating range can be determined in a parameter-free calculation. The numerical results will be for a monatomic and a multi-atom Pd SFM tip interacting with graphite, a system which has been discussed in [11.16].

I will start with a discussion of the minimum load required to observe atomic-scale features in SFM images and/or non-zero friction (Fig. 11.7) on a *rigid* substrate. Figure 11.16a shows the expected SFM corrugation Δz during a horizontal xy scan of the graphite surface by a monatomic Pd tip, for $f_{ext} = 10^{-8}$ N. The top view of the geometry is shown schematically in the inset of Fig. 11.16b for a monatomic Pd tip (left) and a three-atom Pd tip (right) at the hollow ("H") site. The hatched circles correspond to Pd atoms at the tip apex.

Figure 11.16b shows the SFM corrugation $\Delta z(x)$ for different loads f_{ext}. The tip trajectory along the surface x-direction, shown by arrows in the inset of Fig. 11.16b, contains the "T" and "H" sites and yields the largest corrugation. As
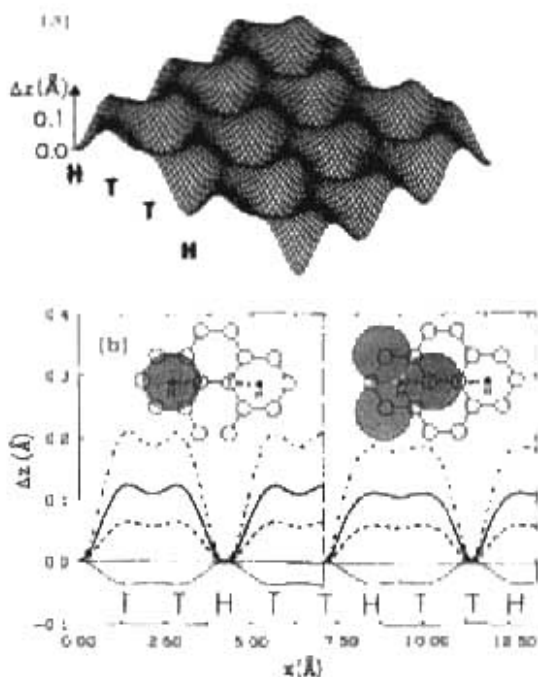
Fig. 11.16. (a) Surface corrugation Δz experienced by a monatomic Pd SFM tip scanning the xy surface plane of rigid graphite under the applied SFM load (per atom $f_{ex} = 10^{-8}$ N (b) Δz (with respect to the "H" site) along the surface x direction for a "sharp" 1-atom tip (left) and a "dull" 3-atom tip (right). The applied loads are $f_{ex} = 10^{-9}$ N (dotted line), 3×10^{-9} N (dashed line), 10^{-8} N (solid line), and 2×10^{-8} N (dash dotted line) The inset shows the geometry of the tip-graphite system in top view. The SFM tip is shown above the hollow site and the shaded area represents Pd atoms [11.16]

discussed in Sect. 11.3.1, the favored surface site changes with changing load. For the sake of simple comparison, Δz (hollow site) is set to zero in Fig. 11.16b which gives a sign change of Δz near $f_{ex} = 2.5 \times 10^{-9}$ N. This calculation indicates that in order to achieve observable atomic resolution in the SFM in the constant force mode, which requires $\Delta z \gtrsim 0.05$ Å, the load on the tip must be $f_{ex} \gtrsim 5 \times 10^{-9}$ N. Since the corrugation Δz along a trajectory connecting adjacent "T" sites is very small (Fig. 11.16b), the observation of individual carbon atoms is unlikely, as has been confirmed by experiment [11.35] Depending on the force constant c in the "realistic friction microscope", a similar minimum load is expected for the onset of non-zero sliding friction (Fig. 11.7) during the scan.

For an n-atom tip which is commensurate with the substrate, the average load per SFM tip atom is $f_{ex} = F_{ext}/n$ and the equilibrium tip height $z_{tip, min}$ can be estimated using (11.18). It should be noted that, under certain conditions, such a "dull" multi-atom tip can still produce atomic corrugation for f_{ex} similar to a monatomic tip This is the case for an ideally aligned tip with a close-packed (111) surface, since the unit cells of Pd and graphite are nearly identical in this case, as shown in the inset of the right-hand side Fig. 11.16b. Thus, for an incompressible substrate, the "sharpness" of the SFM tip need not play a decisive role in the resolution. Of course, a strong suppression of height corrugations and the (horizontal) friction force is expected in the case of large tips which are incommensurate with the substrate. This has been discussed in [11.3] and can be

understood intuitively in the simple-minded haircomb model of sliding friction in Fig. 11.1a.

The range of applicable loads F_{ext} is limited by the condition that substrate distortions near the SFM tip should remain in the elastic region. Since full-scale LDA calculations of local SFM-induced distortions of a semi-infinite graphite surface are practically not feasible, the following approach has proven to be quite useful. For small loads, the relaxation of carbon atoms at the graphite surface due to the SFM tip can be determined using continuum elasticity theory [11.36], with elastic constants obtained from *ab initio* calculations [11.30]. This continuum approach is applicable in the linear response regime and has been successfully used previously to calculate local rigidity, local distortions and the healing length of graphite near an SFM tip and near intercalant impurities [11.30, 36]. In a second step, the total charge density of the distorted graphite substrate is reconstructed from a superposition of atomic charge densities (see (11.14)) which can be calculated by LDA. Based on this total charge density, the tip–substrate interaction and the equilibrium tip position for a given applied load can be obtained using (11.12).

In the continuum elasticity calculation, the semi-infinite system of graphite layers is characterized by the interlayer spacing d, the in-plane C–C bond length d_{C-C}, the flexural rigidity D, the transverse rigidity K (proportional to C_{44}) and c-axis compressibility G (proportional to C_{33}) [11.30, 36]. The LDA calculations for undistorted graphite yield $d = 3.35$ Å and $d_{C-C} = 1.42$ Å, in excellent agreement with experimental and previous theoretical results [11.37, 38]. The continuum calculation is further based on the elastic constants $D = 7589$ K, $K = 932$ K Å^{-2} and $G = 789$ K Å^{-4} which have been obtained from calculated graphite vibration modes [11.30] and the experiment [11.37]. The continuum elasticity theory, as applied to SFM experiments on graphite, is discussed in more detail in Chap. 10.

The total charge density of the graphite surface, distorted by a Pd SFM tip, is shown in Fig. 11.17. A comparison of charge density contours with results of the self-consistent calculation in Fig. 11.10b proves a posteriori the applicability of the linear superposition of atomic charge densities. Fig. 11.17a shows that the substrate distortions in response to a monatomic SFM tip at a load $F_{ext} = f_{ext} = 5 \times 10^{-9}$ N are already substantial, while the corrugations of $\Delta z \approx 0.06$ Å, shown in Fig. 11.16b, are marginally detectable. For larger applied loads $F_{ext} = f_{ext} > 5.0 \times 10^{-9}$ N, which would lead to sizeable corrugations in Δz, the local distortions of graphite are very large. Even though linear response theory is not applicable in this force range, the estimated substrate distortions, shown in Fig. 11.17b, indicate the possibility of tip-induced *plastic* deformations in this load range. As shown in Fig. 11.17c, similar large (and possibly plastic) deformations are expected for a tip with a multi-atom apex, even though the load per atom f_{ext} may be relatively small.

In general, we expect plastic deformations to occur whenever the interlayer distance in graphite approaches the value of the intralayer C–C distance. According to linear response theory, this occurs for $f_{ext} \gtrsim 5 \times 10^{-9}$ N. Under

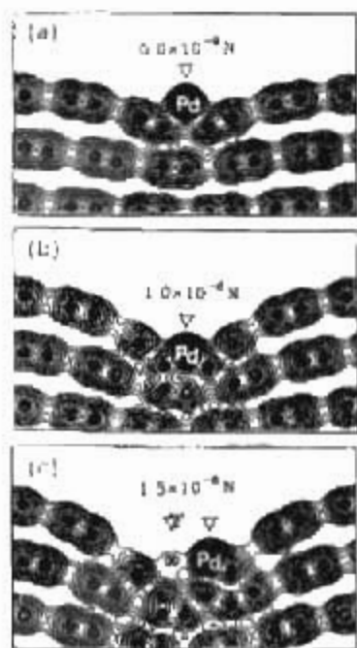**Fig. 11.17.** Total charge density ϱ of a Pd SFM tip interacting with the elastic surface of graphite near the hollow site. Contours of constant ϱ are shown in the ci-plane perpendicular to the surface. The results are for loads (a) $F_{ex} = f_{ex} = 5 \times 10^{-9}$ N and (b) $F_{ex} = f_{ex} = 1 \times 10^{-8}$ N applied on a monatomic tip, and (c) for $F_{ex} = M_{ex} = 1.5 \times 10^{-8}$ N applied on a 3-atom tip. The ratio of two consecutive charge density contours $\varrho(n+1)/\varrho(n)$ is 1.4. The location of the applied load acting on the Pd atoms at the apex of the tip is indicated by $\triangledown$ [11.16].

these conditions, an irreversible rehybridization of carbon orbitals from graphitic sp^2 to diamond-like sp^3 bonding is likely to occur below the tip apex. An estimate of the critical SFM force for this plastic deformation, which does not rely on the continuum elasticity theory, has been obtained in a first-principles calculation [11.39] of the graphite–diamond transition as a function of external pressure along the graphite c axis. These results, corresponding to an "infinitely extended tip", indicate a critical force per surface atom of $f_{cd} = 10^{-9}$ N for this transition. Due to the large flexural rigidity of graphite, this force increases by half an order of magnitude for a one-atom tip, in agreement with the value quoted above.

A realistic SFM tip is more complex than the model tip discussed above and could consist of a micro-tip of one or few atoms on top of a larger tip. A substantial portion of this larger tip could, through the "cushion" of a contamination layer [11.31] or a graphite flake [11.40, 41], distribute the applied load more evenly across a large substrate area, reduce the large curvature near the tip (Fig. 11.17) and increase the minimum separation between graphite layers. This effect would increase the upper limit of applicable loads f_{cr}, compatible with elastic substrate deformations and make nondestructive imaging of surface topographic features and of sliding friction on the atomic scale possible [11.35].

References

11.1   A summary of the present knowledge in tribology can be found in Adhesion and Friction, ed. by M. Grunze, H.J. Kreuzer: Springer Ser. in Surf. Sci., Vol. 17 (Springer, Berlin Heidelberg 1989)

11.2   C. Mathew Mate, Gary M. McClelland, Ragnar Erlandsson, Shirley Chiang: Phys. Rev. Lett. **59**, 1942 (1987)

11.3   G.M. McClelland: In [11.1]

11.4   J. Spreadborough: Wear **5**, 18 (1962)

11.5   R.D. Arnell, J.W. Midgley, D.G. Teer: Proc. Inst. Mech. Eng. **179**, 115 (1966)

11.6   J. Skinner, N. Gane, D. Tabor: Nat. Phys. Sci. **232**, 195 (1971)

11.7   G. Binnig, C.F. Quate, Ch. Gerber: Phys. Rev. Lett. **56**, 930 (1986); ibid. Appl. Phys. Lett. **40**, 178 (1982); G. Binnig, Ch. Gerber, E. Stoll, T.R. Albrecht, C.F. Quate: Europhys. Lett. **3**, 1281 (1987)

11.8   Uzi Landman, W.D. Luedtke, A. Nitzan: Surf. Sci. **210**, L177 (1989); Uzi Landman, W.D. Luedtke, M.W. Ribarsky: J. Vac. Sci. Technol. A **7**, 2829 (1989)

11.9   W. Zhong, D. Tománek: Phys. Rev. Lett. **64**, 3054 (1990)

11.10 L.D. Landau, E.M. Lifshitz: Course of Theoretical Physics, Vol. 1: Mechanics (Pergamon, Oxford 1960) p. 122

11.11 The optimum selection of C is characterized by strong A–C and B–C bonds, while C itself should have a low shear modulus.

11.12 G.A. Tomlinson: Phil. Mag. S. 7, Vol. 7, 905 (1929)

11.13 D. Tománek, W. Zhong, H. Thomas: Europhys. Lett. **15**, 887 (1991)

11.14 E. Meyer, R. Overney, L. Howald, D. Brodbeck, R. Lüthi, H.-J. Güntherodt: In *Fundamentals of Friction*, ed. by I. Singer, H. Pollock: NATO-Advanced Study Institute Series (Kluwer, Dordrecht 1992)

11.15 J.E. Sacco, J.B. Sokoloff, A. Widom: Phys. Rev. B **20**, 5071 (1979)

11.16 W. Zhong, G. Overney, D. Tománek: Europhys. Lett. **15**, 49 (1991)

11.17 W. Kohn, L.J. Sham: Phys. Rev. **140**, A1133 (1965)

11.18 C.T. Chan, D. Vanderbilt, S.G. Louie: Phys. Rev. B **33**, 2455 (1986); C.T. Chan, D. Vanderbilt, S.G. Louie, J.R. Chelikowsky: Phys. Rev. B **33**, 7941 (1986)

11.19 M. Anders, C. Heiden: (submitted for publication)

11.20 C. Horie, H. Miyazaki: Phys. Rev. B **42**, 11757 (1990)

11.21 R. Smoluchowski: Phys. Rev. **60**, 661 (1941)

11.22 This effect is also responsible for the large value of the surface diffusion constant on graphite and apparent small sensitivity of surface friction to adsorbed films, as discussed in [11.6]

11.23 J.B. Pethica, W.C. Oliver: Physica Scripta T **19**, 61 (1987); I.P. Batra, S. Ciraci: Phys. Rev. Lett. **60**, 1314 (1988)

11.24 S. Gould, K. Burke, P.K. Hansma: Phys. Rev. B **40**, 5363 (1989)

11.25 F.F. Abraham and I.P. Batra: Surf. Sci. **209**, L125 (1989)

11.26 D. Tománek, W. Zhong: Phys. Rev. B **43**, 12623 (1991)

11.27 M.S. Daw, M.I. Baskes: Phys. Rev. B **29**, 6443 (1984)

11.28 In the following, I denote microscopic forces per atom by f and macroscopic forces applied on large objects by F

11.29 Near $f_{ext} = 5 \times 10^{-9}$ N, the potential V is essentially constant across the graphite surface, which leads to $\mu \approx 0$ (Fig. 11.14). Small deviations from this behavior can arise due to tip-induced substrate deformations and small inaccuracies in the energy formula given in (11.12)

11.30 D. Tománek, G. Overney, H. Miyazaki, S.D. Mahanti, H.J. Güntherodt: Phys. Rev. Lett. **63**, 876 (1989); ibid. **63**, 1896(E) (1989)

11.31 H.J. Mamin, E. Ganz, D.W. Abraham, R.E. Thomson, J. Clarke: Phys. Rev. B **34**, 9015 (1986)

11.32 L.D. Landau, E.M. Lifshitz: Course of Theoretical Physics, Vol. 7: Theory of Elasticity, (Pergamon, Oxford 1986) p. 53

11.33 S. Ciraci, A. Baratoff, I.P. Batra: Phys. Rev. B **41**, 2763 (1990); I.P. Batra, S. Ciraci: J. Vac. Sci. Technol. A **6**, 313 (1988)

11.34 U. Landman, W.D. Luedtke, N.A. Burnham, R.J. Colton: Science **248**, 454 (1990)

11.35 E. Meyer, H. Heinzelmann, P. Grütter, Th. Jung, Th. Weiskopf, H.-R. Hidber, R. Lapka, H. Rudin, H.-J. Güntherodt: J. Microsc. **152**, 269 (1988)

11.36 S. Lee, H. Miyazaki, S.D. Mahanti, S.A. Solin: Phys. Rev. Lett. **62**, 3066 (1989)

11.37 H. Zabel: In *Graphite Intercalation Compounds*, ed. by H. Zabel, S.A. Solin: Topics in Current Phys. Vol. 14 (Springer, Berlin Heidelberg 1989).

11.38 C.T. Chan, K.M. Ho, W.A. Kamitakabara: Phys. Rev. B **36**, 3499 (1987); C.T. Chan, W.A. Kamitakahara, K.M. Ho, P.C. Eklund: Phys. Rev. Lett. **58**, 1528 (1987)

11.39 S. Fahy, S.G. Louie, M.L. Cohen: Phys. Rev. B **34**, 1191 (1986)

11.40 J.B. Pethica: Phys. Rev. Lett. **57**, 3235 (1986)

11.41 G. Overney, D. Tománek, W. Zhong, Z. Sun, H. Miyazaki, S.D. Mahanti, H.J. Güntherodt: J. Phys.: Cond. Mat. **4**, 4233 (1992)